Automatic detection of common surface defects on oranges using combined lighting transform and image ratio methods

Jiangbo Li, Xiuqin Rao, Fujie Wang, Wei Wu, Yibin Ying*

College of Biosystems Engineering and Food Science, Zhejiang University, 866 Yuhangtang Road, Hangzhou 310058, China

ARTICLE INFO

ABSTRACT

Automatic detection of fruit peel defects by a computer vision system is difficult due to the challenges of acquiring images from the surface of spherical fruit and the visual similarity between the stem-ends and the true defects. In this study, oranges with wind scarring, thrips scarring, scale infestation, dehiscent fruit, anthracnose, copper burn, canker spot and normal surface were researched. A lighting transform method based on a low pass Butterworth filter with a cutoff frequency $D_0 = 7$ was first developed to convert the non-uniform intensity distribution on spherical oranges into a uniform intensity distribution over the whole fruit surface. However, the stem-ends were easily confused with defective areas. In order to solve this problem, different color components (R, G and B) and their combinations were analyzed. It was found that a ratio method and R and G component combination coupled with a big area and elongated region removal algorithm (BER) could be used to differentiate stem-ends from defects effectively. Finally, a processing and classification algorithm based on a simple thresholding method was proposed. The result with 98.9% overall detection rate for the 720 independent sample images indicated that the proposed algorithm was effective in differentiation of normal and defective oranges. The method, however, could not discriminate between different types of defects.

© 2013 Elsevier B.V. All rights reserved.

1. Introduction

Globally citrus is an important horticultural product, and in China its annual production is over thirty million tons. In many countries, much of the sorting and grading process is not automated. In recent years commercial machine vision systems have been widely applied to evaluate external quality of fruit. However, these systems cannot provide robust and accurate results because of the high variability of defect types and the presence of stem-ends and calyxes. For this reason, packinghouses demand more advanced systems with more complex image processing algorithms (Aleixos et al., 2002; Blasco et al., 2007a).

In general, many fresh fruits, such as oranges, apples, peaches and pears, are approximately spherical. One concern for image acquisition of spherical and curved fruit is that lighting reflectance is not uniformly distributed (Tao, 1996). This generally results in a darkening of the edges of the object, while the central part appears brighter (Aleixos et al., 2002). Moreover, this darkening of the edges can even lead to this area of sound peel frequently being mistaken for damaged skin (Gómez-Sanchis et al., 2008). Therefore, research has been conducted to address the issue by using proper lighting systems to provide uniform spatial illumination for fruit. Yang (1993) used a combined structured and diffuse lighting system to detect defects and the stem-end and calyx on apples. Leemans et al. (1998) used devices equipped with lighting tubes, diffusers and reflectors to provide uniform irradiance. Kleynen et al. (2005) designed a lighting tunnel including two different light sources for detecting defects on apples. In general, an effective lighting system may prevent the healthy surfaces near the boundary from being classified as defective areas and prevent the defective areas near the object's center from being detected as good surfaces (Tao and Wen, 1999; Gómez-Sanchis et al., 2008). However, the many natural variations of fruit, such as size, shape, texture and color, make it difficult to establish a universal lighting system that will be effective for all fruits and in all kinds of situations. Moreover, the system of illumination can also not be optimal designed due to mechanical, spatial, or cost limitations. Kleynen et al. (2005) advised to remove vignetting on the images by using 'flat field correction'. Unay and Gosselin (2007) reported that segmentation was problematic at the far edges of fruit probably due to illumination artifacts. Therefore, the outline of the fruit was eroded to alleviate this problem; but this method involves a loss of quality in the inspection, because sometimes an important part of the fruit surface is not analyzed. Another solution that has traditionally been employed is local thresholding (Blasco and Moltó, 2002). This method assumes that central areas and edges belong to

---

* Corresponding author. Tel.: +86 0571 88982885.
   E-mail address: ybying@zju.edu.cn (Y. Ying).

different regions of interest. Although this method may extract defects, it requires a longer processing period (Tao and Wen, 1999). Since studying the different relations linking two and more RGB channels may alleviate the effect of uneven illumination (Unay and Gosselin, 2007), most inspection systems only use color features to segment the defects. However, non-uniform reflectance intensity distribution from spherical fruit surfaces also exists on color images and affects the correct detection of defects. In order to effectively extract defective areas from an image of spherical fruit, it is essential to eliminate any negative influence produced by the lighting system or image acquisition device. Hence, the fruit reflectance must be corrected.

In order to differentiate the stem-ends and calyxes from defects, many efforts also have been made using both mechanical and machine vision technology (Sarker and Wolfe, 1985; Throop et al., 2001; Bennedsen and Peterson, 2005). However, variations in fruit size, shape, and surface curvature appear to play a role in fruit orientation. Therefore, mechanical solutions are not considered in this paper. In earlier studies, some researchers used structured lighting to detect the stem-end and calyx. Localization of the stem-end and calyx was achieved by detecting deformations of the lighting patterns (Yang, 1993, 1996; Crowe and Delwiche, 1996a, 1996b). However, due to the randomness of the moving fruit, it is very difficult to detect the deformations of the lighting patterns on the fruit surface. Wen and Tao (2000) built a dual-camera imaging system to identify apple stem-end and calyx by comparing the NIR and MIR images. Although an accuracy of 99% was achieved, cost of cameras, which is not discussed by the authors, is an important issue for practical implementation of this approach. Other approaches were based on more complex image processing methods. Li et al. (2002) assumed that stem-end and calyx areas were concave and a defective one would have lost its concavity. Fractal analysis with an artificial neural network was used to discriminate stem-ends and calyxes from true defects. The results showed that highly rotten areas were easily misclassified because their surfaces were concave. Ying et al. (2003) proposed an algorithm to detect the stem-ends of pear. The stalk was assumed to be a protrusion of the spherical fruit. However, that study was more interested in detecting the length of stalks than sorting between stem-ends and defects. Recently, Unay and Gosselin (2007) compared linear discriminant, nearest neighbor, fuzzy nearest neighbor, and support vector machine classifiers. Support vector machine, which was found to be the best among all classification algorithms tested, correctly recognized 99% of the stem-ends and 100% of the calyxes using a selected feature subset. Zhu et al. (2007) introduced a three-dimension (3D) shape reconstruction approach for identifying stem-ends and calyxes. One great obstacle with 3D technology is that reconstruction of every fruit surface is time-consuming owing to complex algorithms.

The above literature review reveals that defect detection, especially differentiating between stem-ends, calyxes, and defects, are a necessary task for an effective fruit sorting system, but it is not easy to accomplish. These studies provide good references and resources for dealing with various problems associated with detection of citrus surface defects and stem-ends. However, citrus fruit also have some unique features, especially stem-ends, compared to apples, pears, and other kinds of fruit. Therefore, there is a need to specifically study citrus defects and stem-ends. Recce et al. (1998) used a neural network classifier to distinguish the true defects from the stem-ends of oranges. Quite poor results were obtained. Aleixos et al. (2002) developed a multispectral camera system that could acquire visible and near infrared images from the same scene to detect defects on citrus. Leemans and Destain (2004) compared defect segmentation results of three models that were generated using the RGB, RGI and RGBI. The RGBI model, which was found to be the best, correctly recognized 100% of the

stem-ends and 99.1% of defects based on Bayesian classification algorithm. In a recent study, Blasco et al. (2007a) developed an unsupervised growing region algorithm to detect citrus surface defects, assuming that in a fruit with peel defects, the larger region corresponded to the sound peel and smaller areas were defects. Kim et al. (2009) used 14 color texture features of grapefruit peel diseases to classify defects based on an HSI model. López-García et al. (2010) developed an algorithm, which was based on multivariate image analysis and principal component analysis to detect the defects on citrus fruit surfaces. The success ratio for the detection of individual defect was 91.5%. These approaches include supervised and unsupervised methods. The quick processing speed of supervised methods, such as neural network and Bayesian methods, allows their implementation in processes that require fast working speed, such as on-line inspection of citrus fruit. However, the wide diversity of defect types means that automatic inspection systems have to be frequently retrained in order to adapt the inspection to these changes. Although unsupervised methods, such as a growing region algorithm, can avoid the problem of frequent system retraining, the complexity of these algorithms restrains the detection speed. Moreover, the above-mentioned methods cannot avoid the influence of sorting and inspecting citrus fruit images that have non-uniform reflectance intensity distributions caused by the curved shape. In addition, although some reports give better segmentation results for defects and stem-ends on citrus fruits (Aleixos et al., 2002; Blasco et al., 2007a; López-García et al., 2010), how to discriminate between stem-ends and true defects has not been reported.

2. Objective

The objective of this work was to develop an effective combination algorithm for detecting the common defects on oranges. To achieve this objective, a lighting transform method and stem-end identification approach was proposed in this study, respectively. The proposed combination imaging algorithm should not only solve the problem of sorting and inspecting fruit images having non-uniform reflectance intensity distribution caused by the curved shape, but also eliminate the adverse effects produced by the similarity between stem-ends and defects.

3. Materials and methods

3.1. Fruit samples

'Newhall' variety oranges were selected for study because their automatic inspection is challenging for the agro-food industry and because they have nearly spherical shape with a very reflective surface. The orange samples were hand picked from the commercial orchard in Jiangxi during the harvest season from December 2009 through January 2010. The peel conditions of fruit were visually classified by fruit grading experts. Fruit samples with normal surface and seven common defective peel conditions (i.e., wind scarring, thrips scarring, scale infestation, dehiscent fruit, anthracnose, copper burn and canker spot) were collected. Defect sizes varied from large defects, such as anthracnose, to small ones like scale infestation. The color also differed from one to another and ranged from the gray of thrips scarring, the brown of copper burn to the black of anthracnose. Representative images for each peel condition are shown in Fig. 1.

All samples were washed and treated with chlorine and sodium o-phenylphenate (SOPP) at the Machine Vision Lab of the College of Biosystems Engineering and Food Science, Zhejiang University, Hangzhou. These samples were then stored in an environmental control chamber maintained at 5 °C and they
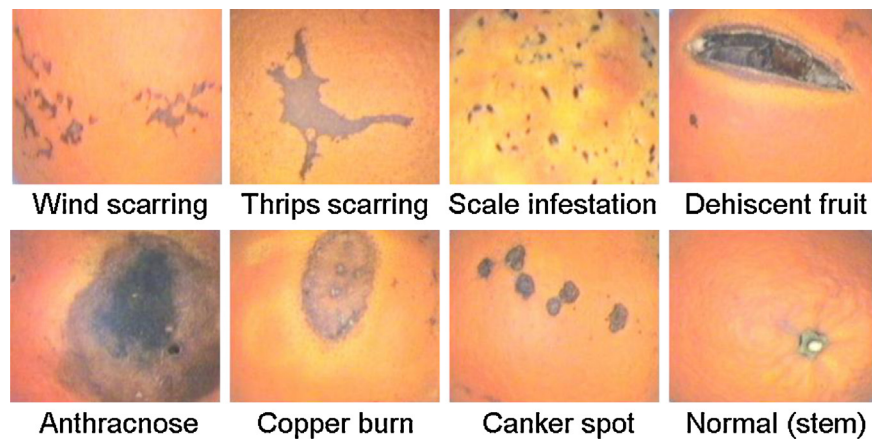
Fig. 1. Representative normal and defective peel conditions of orange samples.

were removed from cold storage about 2 h before imaging to allow them to reach room temperature. Sixty samples for each peel condition were selected and two images of each sample were acquired, hence a total of 960 orange images were tested in this study.

3.2. Image acquisition

The color image acquisition system used in the study was composed of a color CCD camera (Pulnix TMC-7DSP) and a frame grabber (Matrox Meteor II), connected to a personal computer [Pentium 2.00 GHz, 256 Mb RAM (random access memory)]. The illumination system consisted of six fluorescent tubes (F40BX/840, 20 W each). Diffuse reflection plates were placed in front of the fluorescent tubes to reduce the bright spots on the images. The camera and the lighting system were placed inside the inspection chamber. The inspection chamber is 1300 mm in height, 660 mm in width and 680 mm in length. The camera was placed about 900 mm from the top of the fruit. Using this configuration (shown in Fig. 2), images containing one fruit were acquired off-line. The size of the acquired images is 640 by 480 pixels with a resolution of 0.28 mm/pixel. During image acquisition, the orange was placed on a blue background plate, manually orienting the side of fruit that contained the regions of interest (ROI) toward the camera. Each image was saved in TIFF (tagged image file format) with a name related to the type of peel and number of image.

3.3. Background segmentation

A binary mask to produce an image containing only the fruit, avoiding any interference from the background that could reduce discrimination efficiency was produced. In this work, the blue (B) component image was chosen to build the binary mask because the contrast between the fruit and the background in the image was maximum. More importantly, it was observed that the B component was insensitive to all studied defects. Fig. 3 shows the original RGB image (a) of an orange with canker spots, B component image (b), and the B component histogram (c). It can be seen that the histogram is clearly bivalued, a condition that facilitates an optimal segmentation of fruit and background. The mask (d) was then obtained by applying a simple thresholding method to the B component image. Finally, the mask was used to remove the image background.

3.4. Lighting transform method

Images are typically described by two-dimensional functions of the form $f(x,y)$. The function $f(x,y)$ may be characterized by two components: (1) the amount of source illumination incident on the scene being viewed, and (2) the amount of illumination reflected by the objects in the scene. Appropriately, these are called the illumination and reflectance components and are denoted by $i(x,y)$ and
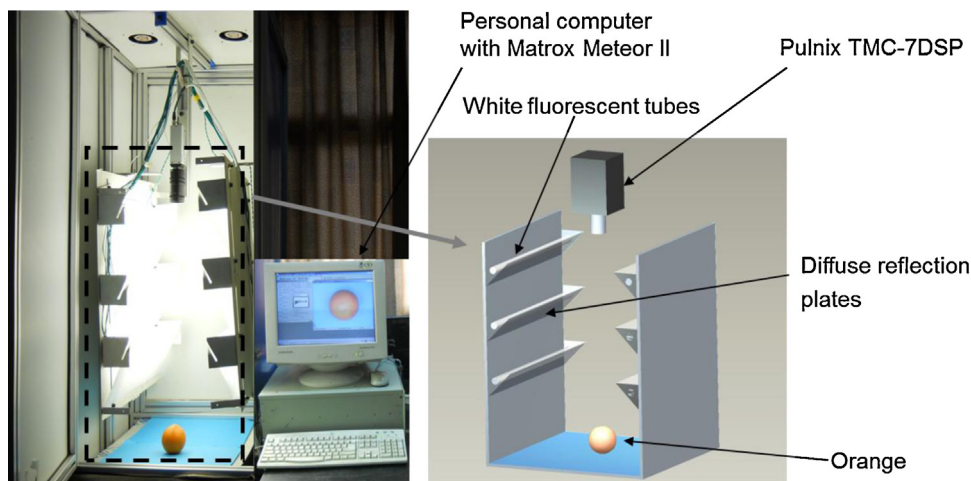

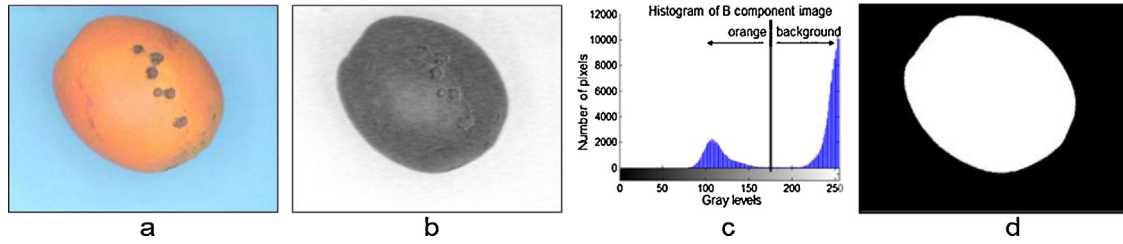**Fig. 2.** Scheme of the image acquisition system.

Fig. 3. (a) Original RGB image with canker spots, (b) B component image, (c) histogram for thresholding and (d) mask obtained after thresholding.

$r(x,y)$, respectively. The two functions combine as a product to form $f(x,y)$ (Gonzalez and Woods, 2010):

$$f(x, y) = i(x, y)r(x, y) \tag{1}$$

The illumination component of a fruit image generally is characterized by slow spatial variations, while the reflectance component tends to vary abruptly, particularly at the junctions of dissimilar regions. These characteristics lead to associating the low frequencies of the Fourier transform of an image with illumination and the high frequencies with reflectance. The low frequency component of an image can be obtained by the following steps:

(1) Multiply the input image by $(-1)^{x+y}$ to center the transform and compute Fourier transform $F(u,v)$ by the following equations:

$$\mathfrak{I}[f(x, y)(-1)^{x+y}] = F\left(\frac{u - M}{2}, \frac{v - N}{2}\right) \tag{2}$$

where $\mathfrak{I}[\bullet]$ denotes the Fourier transform. Multiplying $f(x,y)$ by $(-1)^{x+y}$ shifts the origin of $F(u,v)$ to frequency coordinates $(M/2,N/2)$, which is the center of the $M \times N$ area occupied by the two dimensions discrete Fourier transform.

(2) The Fourier transform of the output image is given by:

$$G(u, v) = H(u, v)F(u, v) \tag{3}$$

where $G(u,v)$ is Fourier transform of the output image; $H(u,v)$ is the low pass filter function; and, $F(u,v)$ represents the Fourier transform of the input image.

The $H(u,v)$ was used to obtain the low frequencies that represent illumination information in the image. A Butterworth low pass filter of order 1 was used because it has no ringing and it has strong adaptability compared to an ideal low pass filter or Gaussian low pass filter (Gonzalez and Woods, 2010). The filter was defined as:

$$H(u, v) = \frac{1}{1 + (D(u, v)/D_0)^2} \tag{4}$$

$$D(u, v) = \left[\left(\frac{u - M}{2}\right)^2, \left(\frac{v - N}{2}\right)^2\right] \tag{5}$$

where D_0 is the cutoff frequency; and, $D(u,v)$ is the distance from any point (u,v) to the center (origin) of the Fourier transform.

(3) The low frequency component image $g(x,y)$ was obtained using:

$$g(x, y) = \{real[\mathfrak{I}^{-1}[G(u, v)]]\}(-1)x + y \tag{6}$$

where $\mathfrak{I}^{-1}[\bullet]$ denotes the inverse Fourier transform; The real part is selected in order to ignore parasitic complex components resulting from computational inaccuracies (Gonzalez and Woods, 2010).

Once the $g(x,y)$ is generated, the corrected image $f'(x,y)$ is given by:

$$f'(x, y) = \frac{f(x, y)}{g(x, y)} \times 255 \tag{7}$$

The $f(x,y)$ is basically a plane image with defects below the plane in gray levels. The binary image $d(x,y)$, with only defects, can be easily obtained by performing the following global threshold operation:

$$d(x, y) = \begin{cases} 0 & if \quad f'(x, y) > T \\ 1 & otherwise \end{cases} \tag{8}$$

where T is the threshold setting at or near the flat plane in the $f(x,y)$. The threshold is selected manually and is user-adjustable in practical application. However, once the threshold is selected, it was applied to all tested images.

In this study, 240 sample images (30 images for each skin condition) were randomly selected from 960 images as training set to develop the lighting transform algorithm. The remaining 720 sample images (90 images for each skin condition) were used as test set to estimate the performance of algorithm.

3.5. Stem-end identification algorithm

Stem-end detection is the most difficult step in the process of grading fruit, since these natural parts of fruit normally present similar intensity levels to true defects. However, as shown in Fig. 1, the stem-end of citrus fruit has two very important features compared to the stem-end of other fruits, such as apple. On the one hand, the stem-end areas of citrus fruit do not have a deeply concave shape. This feature makes stem-ends easier to be detected regardless of its relative location in the image. On the other hand, the detection and grading of oranges is usually performed shortly after picking, especially for detecting defects, because defective oranges easily rot and infect other normal fruit with time. Therefore, citrus fruit stem-end is generally greener than other types of peel defects and normal peels during the grading process. Therefore, a stem-end identification algorithm was developed based on studying different components (R, G and B) and their combinations in this work. As a first step, the region of interest (ROI) images of all types of defects and stem-ends were manually segmented from original RGB images by a fruit grading expert. Generally, the ROIs were smaller than actual defective areas and stem-ends. Each ROI image (RGB image) was saved in TIFF with a name related to the peel types.

A total of 960 orange images were divided into two groups: the 'images with stem-ends' group included 331 sample images with normal and defective peels and the 'images without stem-ends' group including 629 sample images with normal and defective peels. 480 sample images (60 images for each skin condition) including 163 images with stem-ends and 317 images without stem-ends were randomly selected for developing stem-end identification algorithm. The rest of the images (480) were used to evaluate the performance of algorithm. Table 1 details the selected images for developing and evaluating algorithm.

120 ROI images were obtained from 60 different color images (two ROIs per image) for every kind of peel defect and sound

Table 1
Image selection based on different type of peel condition for stem-end identification algorithm.

Type of peel	Images with stem-end (331)		Images without stem-end (629)		Total
	Developing algorithm	Evaluating algorithm	Developing algorithm	Evaluating algorithm	
Wind scarring	28	29	32	31	120
Thrips scarring	10	11	50	49	120
Scale infestation	19	20	41	40	120
Dehiscent fruit	21	21	39	39	120
Anthracnose	15	16	45	44	120
Copper burn	20	20	40	40	120
Canker spot	24	24	36	36	120
Sound surface	26	27	34	33	120
Total	163	168	317	312	960

surface condition. In addition, 326 ROI images were extracted from 163 stem-ends (two ROIs per stem-end). Hence, a total of 1286 ROI images were extracted for developing the algorithm. Afterwards, the gray mean value (MV) of R, G or B component of every type of ROI image was calculated by using the following equation:

$$MV_C = \frac{\sum_{i=1}^{120} \bar{C}_i}{n} \tag{9}$$

where n equals 120 for normal and defective peel conditions and 326 for stem-end; C represents the R, G, or B component of the ROI image, respectively; i is number of every type of ROI image; $\bar{C}$ is an intensity average of the R, G or B component of every ROI image, respectively; MV is the gray mean value of $\bar{C}$.

Table 2 shows that the mean values (MV) of the R, G, B components and combination of R and G components, respectively. As shown in Table 2, it is very difficult to distinguish stem-ends from defects only depending on MV_R intensity information. However, single MV_G or MV_B values have some potential for segregation stem-ends from the rest. However, it was found that the results obtained by only using a single component were sensitive to lighting conditions. The ratio values between the sum of MV_R and MV_G and their difference showed promise for classifying stem-ends, as can be seen from the fourth column in Table 2. Other component combinations for effectively identifying stem-ends might exist, but were not found in this analysis. The 'Original' was the original ratio value (ORV). The 'Normalization' was the normalized value (NV) from ORV. The 'Normalization' was performed as:

$$NV = \frac{ORV}{ORV_{max}} \tag{10}$$

where NV is the normalized value; ORV is the original ratio value, and ORV_{max} is the maximum value of ORV.

As shown in Table 2, the ratio algorithm, based on the R and G components, can be used to discriminate stem-ends from true

defects except for anthracnose and dehiscent fruit. The ratio images (RI) were obtained by using the following equation:

$$RI = \frac{R + G}{\lambda(R - G)} \times 255 \tag{11}$$

where R and G correspond to the R and G components of the original RGB image, respectively; λ is a constant which is user-adjustable according to surface illumination of the original RGB images. In this work, λ is equal to 20, which is selected based on visual assessment of all ratio images with different types of defects and stem-ends.

For most orange samples with dehiscent damage and anthracnose, the defective regions appeared as irregular, elongated, and big regions. However, the shape of the stem-end is more regular and small, and appears as a circular area. Therefore, a big area and elongated region removal algorithm (BER) was applied (Xing et al., 2005). In order to obtain the big areas, the stem-end binary image was obtained and marked. Then, the area of each marked region was computed. If the area was bigger than 285 pixels (Note that a stem-end region varies in size from 164 to 283 pixels in this study), this region was considered as a big area (defect) and removed. Otherwise, the region was retained and further evaluated for being an elongated region. An elongated region was chosen based on a ratio value related to the diameter of inscribed circle of one region. The inscribed circle was calculated as:

$$d = \frac{4S}{L} \tag{12}$$

where d is the diameter of the inscribed circle of one region; S is the area of the region, and L is the perimeter of the region. S is obtained by computing the pixel sum of the marked region. To obtain the L, the contour of the marked region was extracted. Then, the pixel sum of the contour was computed as L. The units for these parameters are in pixels.

The inscribed circle diameter was then divided by the larger one between the height and width of the region. The height and width is obtained using the minimum out-connected rectangle method based on functions 'regionprops' and 'boundingbox' in MATLAB toolbox. Since most stem-ends appear as regular approximately

Table 2
The mean values (MV) of R, G, B components and combination of different types of defects and stem-ends.

| Type of peel	MV_R	MV_G	MV_B	$(MV_R + MV_G)/(MV_R - MV_G)$	
				Original	Normalization
Wind scarring	189.6	127.1	105.6	5.1	0.29
Thrips scarring	181.5	127.0	101.8	5.7	0.32
Scale infestation	186.3	133.7	95.2	6.1	0.35
Dehiscent fruit	152.5	125.5	105.9	10.3	0.59
Anthracnose	120.0	107.1	102.4	17.6	1.00
Copper burn	160.9	123.9	102.9	7.7	0.44
Canker spot	172.1	132.1	106.9	7.6	0.43
Sound surface	205.3	133.2	108.7	4.7	0.27
Stem-end	179.2	159.3	129.2	17.0	0.97
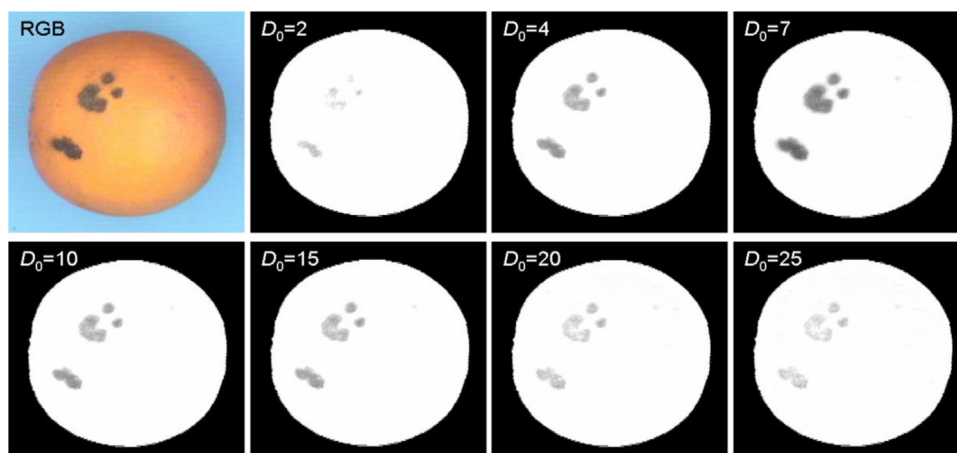
Fig. 4. The corrected images under different D_0.

round areas, the ratio of a true stem-end region will be bigger than that of the region of dehiscent damage or anthracnose. Alternatively, if the ratio of one region is smaller than a threshold value, that region was considered as an elongated area.

3.6. Defect detection algorithm

In this work, the final defect detection algorithm was developed by combining the lighting transform and stem-end detection methods. A mask template was created using the B component. The R component and G component were masked using this template to remove the background. The R component was corrected by the proposed lighting transform method. The ratio image was obtained by using R and G components in order to identify the stem-end. Based on the ratio image, a simple thresholding method with a global threshold value of 0.8 and the BER were applied to extract the stem-end from the other peels, both sound and defective. Finally, the binary stem-end image and corrected R component image were used to obtain the corrected image without stem-end. Once the addition image was obtained, only truely defective areas were extracted by subjecting the addition image to a simple thresholding method.

In addition, morphological filtering was also used with an aim to remove undesired small size pixels (noise) in the resultant binary image. A one-step morphological opening operation, based on a rectangle structuring element with a 2×2 kernel size in MATLAB morphological filter tools, was used in this study and defined as erosion of the image by the structuring element, followed by a dilation of the result by the same structuring element. A structuring element with a 2×2 kernel size was selected considering its effectiveness for removing the noise and retaining some small defects like scale infestation in a defect binary image.

All algorithms presented in this paper were programmed using Matlab 2008a (The MathWorks Inc., Natick, USA) without any special toolbox for the code implementation.

4. Results and discussion

4.1. Lighting transform

In order to choose the optimal cutoff frequency, D_0, used in the illumination correction algorithm, the corrected images under different D_0 were visually assessed. Fig. 4 shows an example of cankerous orange with different D_0. Seen from Fig. 4, a different D_0 could result in different correction results. The contrast between defective areas and normal peel gradually increases from $D_0 = 2$

to $D_0 = 7$ and decreases from $D_0 = 7$ to $D_0 = 25$. The best correction performance was obtained when D_0 equaled 7. From studied 240 sample images (training set), the same correction performance was observed. Therefore, cutoff frequency $D_0 = 7$ was selected for Butterworth low pass filter (Fig. 5).

A typical example of the illumination correction algorithm is shown in Fig. 6. In the first image (Fig. 6a) no correction (original R component of RGB image) has been applied. In contrast, the third image (Fig. 6c) has been corrected by applying the lighting transform method proposed here. The second image (Fig. 6b) is the low frequency component image, called the lighting mask, obtained from Fig. 6a. Before applying the correction method, it can be observed that the image is darker in the peripheral areas of the fruit than in the central part due to the spherical geometry of fruit reflecting a greater amount of radiation toward the camera at the zenith than in the equatorial area (Gómez-Sanchis et al., 2008). After obtaining the lighting mask and applying it to original image, the fruit displayed a uniform intensity distribution over the whole surface and preserved the defects, as shown in Fig. 6c.

This fact is even more apparent in Fig. 7, which represents the gray level profile corresponding to a horizontal line transecting one canker spot in the three images shown in Fig. 6. The profile (in black) corresponding to the uncorrected image illustrates the changes in intensities due to non-uniform intensity distribution. The profile (in red) corresponding to the lighting mask shows a similar intensity distribution, which is lower at the edges and greater in the part near the center. The same figure also shows the profile for the fruit after correction (in blue). In this case it is considerably flatter than the profile of the uncorrected image. Although the intensity level
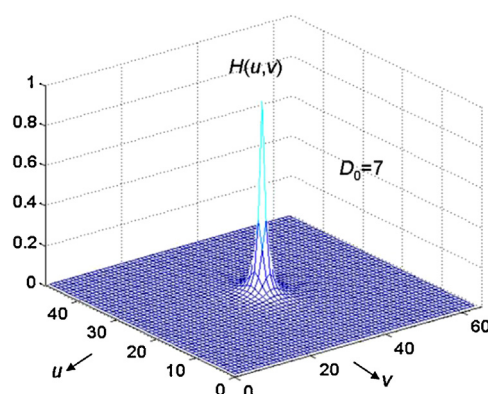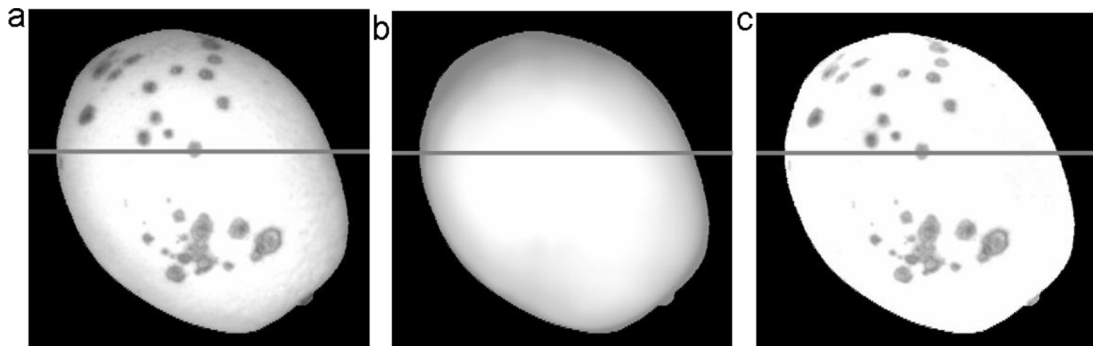

Fig. 5. Butterworth low pass filter.

Fig. 6. (a) Uncorrected original image, (b) lighting mask and (c) corrected image of a orange with canker spots.

near the center surface is saturated due to the curved fruit shape, it does not affect the performance of correction algorithm. Similar results were obtained for 240 sample images (training set) in this study.

Fig. 8 uses another point of view to more clearly illustrate the correction effectiveness of the proposed algorithm. Fig. 8a shows the intensity distribution of the uncorrected original image (Fig. 6a). Different colors correspond to different gray levels. From mazarine blue to dark red, the gray level gradually increases. Note that the defective regions in Fig. 8a have relatively lower intensity values than the healthy surfaces. However, the intensity gradient along the radius of the fruit causes the intensity value of the healthy surface near the boundary to be equal or even lower than the intensity of the defective area near the center of fruit. In contrast, Fig. 8b shows the intensity distribution over the whole fruit surface after correction. As show in Fig. 8b, the intensity levels (in yellow or red) of the edges of spherical fruit are converted to a similar intensity level to the normal center surface (in dark red). The corrected image has no loss of defects (in yellow) on the whole fruit surface. It was also noticed that much of the uncorrected image areas in Fig. 8a were saturated. Usually, image saturation does not affect the effectiveness of the algorithm. However, if the image is supersaturated, it may affect some minor defects such as wind scarring detection because these defects will be difficult to be observed in the original (uncorrected) R component images.

An example of defect segmentation for each defect type based on proposed lighting correction method is shown in Fig. 9. First row corresponds to the original RGB images, second and fourth rows show the defects marked manually using a graphical tool in the original RGB images and corrected images respectively, third row is lighting masks obtained from R components of original RGB

images, and fifth row shows the segmented binary defect images obtained by subjecting the fourth row images to a simple thresholding method using a global threshold value.

As seen, although the detected defective areas do not precisely fit the defects marked manually (second row), the encouraging segmentation results were good enough to perform the inspection task. However, it also should be noted that the method here was basically to apply a low pass Butterworth filter to the fruit image and remove all the details such as defects on the fruit surface. These defect marks that were relatively higher frequency components were removed by selecting a cutoff frequency in the transformed image in the frequency domain. This method was workable for small dots, tracks, or high contrast marks on the fruit surface. However, it may be deficient for larger and very smooth spots, which have low frequency and may be difficult to be removed by the low pass filter. This can be seen from images in Fig. 9 at column 6, where the large and uniform defect area has not been effectively corrected. How to solve this problem is the aim of future research.

To estimate the effectiveness of the lighting transform method, 720 sample images (test set) were processed. Afterwards, the number of the actual defects and the correctly detected defects for each sample were counted. Table 3 shows these results for all samples used in the experiments. 'Number of actual defects' column shows the number of defects that the expert found and manually marked in original RGB images. 'Number of detected defects' column was the number of defects that the expert found in the fruit and which were detected by the method. Sound peel areas mistakenly identified as defects by the method is shown in the table as 'False detections'. As shown in Table 3, an accuracy of 93.1% was achieved with only 3.3% false detection for defective areas. Most undetected defects correspond to wind scarring (9.9%), scale infestation (8.7%) and thrips scarring (5.6%). In the case the undetected wind scarring, the amount of visible damage was so slight that it was only barely apparent on the orange surfaces. Thus, the intensity difference between defective and sound skin areas was too small to be detected by the algorithm. The case of scale infestation is different. Due to the small size of scales, some scales that are
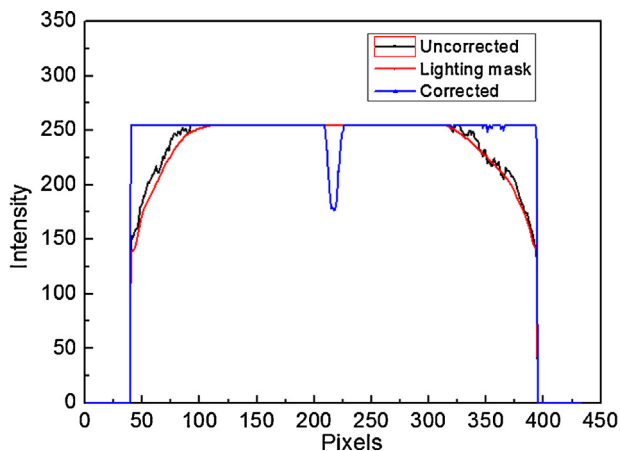

Fig. 7. Spatial intensity profile for the gray level lines transecting one canker spot.

Table 3
Detection results according to the type of each defect for independent test images.

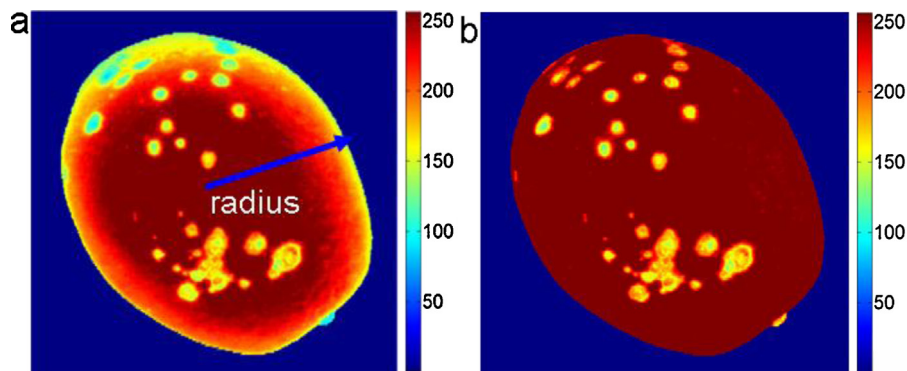| Type of defect	Number of actual defects	Number of detected defects	False detection
Wind scarring	365	329 (90.1%)	17 (4.5%)
Thrips scarring	143	135 (94.4%)	4 (2.7%)
Scale infestation	2743	2504 (91.3%)	92 (2.3%)
Dehiscent fruit	117	113 (96.6%)	3 (2.5%)
Anthracnose	182	182 (100.0%)	8 (4.2%)
Copper burn	90	90 (100.0%)	4 (4.3%)
Canker spot	630	621 (98.6%)	16 (2.5%)
Total database	4270	3974 (93.1%)	144 (3.3%)
Stem-end	251	251 (100.0%)	5 (2.0%)

Fig. 8. (a) Intensity distribution over the whole fruit surface before correction and (b) intensity distribution over the whole fruit surface after correction.

smaller than 1 mm were also removed when the one-step morphological opening operation was used to remove the noise in resultant binary images. In terms of undetected thrips scarring, the intensity of their R components is close to that of the sound skin because these damages are colored in off-white. Thus, the algorithm failed to differentiate between them.

4.2. Stem-end detection

It was also noticed that the lighting transform method does not discriminate stem-ends, which were detected in 100% of the cases, from true defects due to similar intensity. The stem-end identification algorithm developed in this study was able to make this distinction. An example of stem-end identification based on the proposed stem-end detection method is shown in Fig. 10. The first row corresponds to the original RGB images, second row shows the defects marked manually using a graphical tool, middle row shows the ratio images (RI) obtained by using Eq. (11), and the fourth row shows the binary stem-end images after applying thresholding to the ratio images in the middle row.

The effects of the BER algorithm can be seen in the bottom row of Fig. 10. After applying the BER algorithm, the big areas and elongated regions, such as dehiscent damage and anthracnose, were removed by replacing the values of the regions with zeros. Only stem-end areas remained as white spots in the binary images. Another 480 orange images (60 images for each skin condition), including 168 images with stem-ends, were used to test the performance of the stem-end identification algorithm. The distribution of the sample images is shown in Table 1. As shown in Table 4, the 100% recognition rate shows that the stem-end identification algorithm effectively isolates stem-ends from defective areas and normal peel.
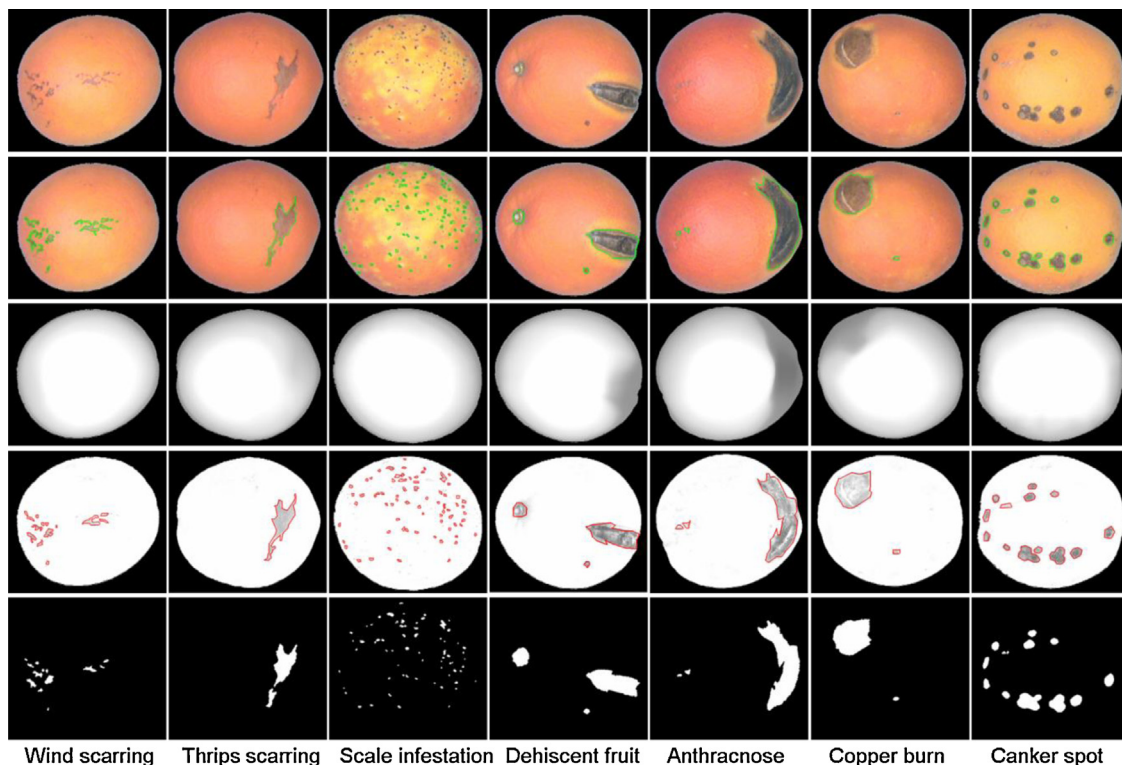

Fig. 9. Example of defective areas segmentation. Original RGB images (first row), manually marked defects in green (second row), lighting masks (third row), manually marked defects after lighting correction in red (fourth row) and binary defect images (fifth row).
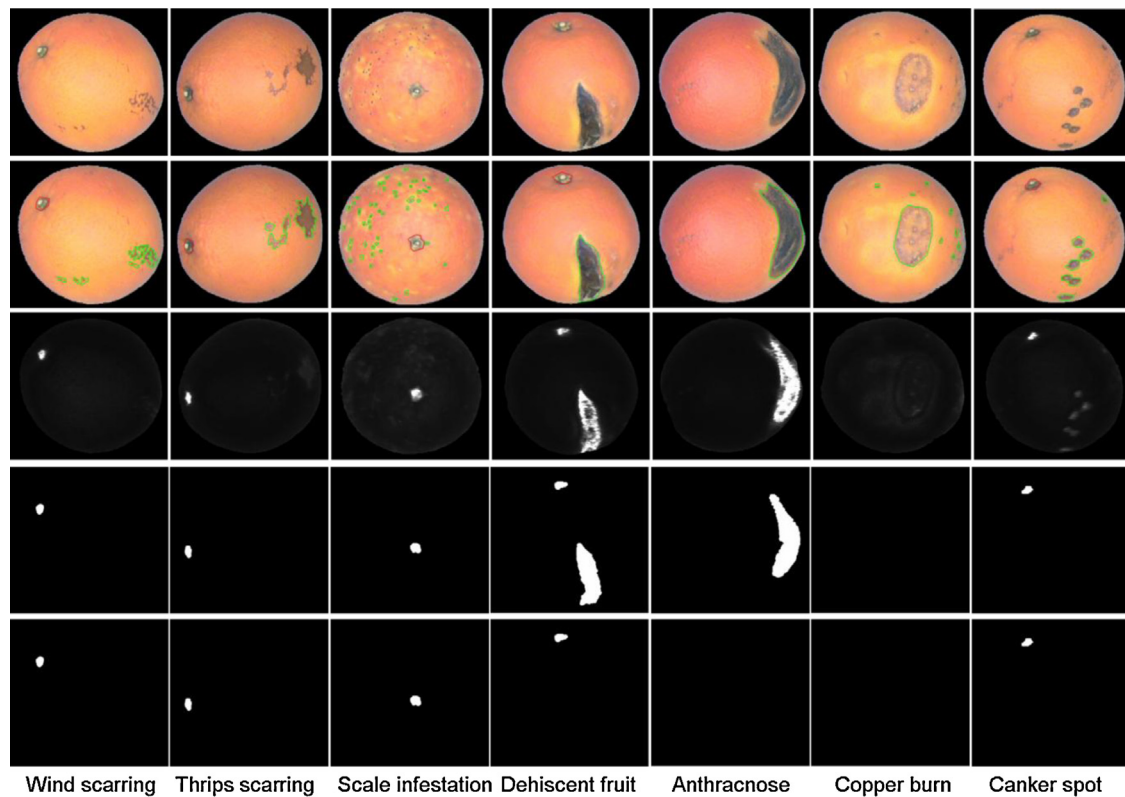
Fig. 10. Example of stem-end detection. Original RGB images (top), manually marked defects in green (second row), ratio images (middle), binary stem-end images after applying thresholding (forth row) and binary stem-end images after applying BER (bottom).

4.3. Defect detection

As described above, defects and stem-ends can be identified clearly in the lighting transform images. Stem-ends can be separated from the true defects and sound skin using the proposed stem-end identification algorithm. However, it is difficult to choose only one algorithm to effectively achieve the defect detection. Fig. 11 photographically demonstrates primary procedures for defect detection using an orange sample with stem-end and thrips scarring on the fruit peel based on the combination algorithm described in Section 3.6.

In this study, the approach of combining both lighting correction and stem-end identification was evaluated using 720 orange sample images from test set. Detection rates for both good and defective fruit were affected by changing the threshold. The detection rate increased with the sorting threshold for defective fruit, but decreased for the good fruit. Table 5 gives the detection results for three representative thresholds. The value of T_3 provided the best overall detection accuracy with 99.0% of the defective samples correctly recognized as defective, and 97.8% of the 90 sound samples correctly recognized as sound. A total of 10 samples were misclassified, and the overall detection accuracy for all the samples was 98.9%. However, from the economic standpoint, slight damage only affects fruit appearance and can be marketed as second

quality (Blasco and Moltó, 2002). The threshold of T_1 can be used to achieve this goal. Using this threshold (T_1), all tested samples were divided into two classes: 'Serious defects' including dehiscent fruit, anthracnose, and canker spot, and 'other' class including wind scarring, thrips scarring, scale infestation, copper burn and sound fruit. Note that the canker spot was considered as a serious defect because this disease can affect the peels of most commercial citrus varieties and cankerous fruit are prohibited from exporting to some 'canker-free' areas such as the European countries (Balasundaram et al., 2009; Qin et al., 2009). As expected, 97.0% of the fruit images with serious defects and 100% of the sound fruit were correctly detected. 2.2% of fruit images with slight defects were misclassified as fruit images with serious defects. In other words, 97.8% of fruit images with slight defects were classified as sound fruit. Since it is impossible to discriminate sound fruit from fruit with slight defects by using the single threshold, T_1, a subsequent sorting using a more discriminating threshold was examined. The classification results found from applying the threshold, T_2, to the 450 sample images including 90 images with sound peel and 360 images with slight defects, are listed in Table 5. 94.4% of slight defects were correctly detected and an accuracy of 100% was achieved for sound fruit. The high detection rates demonstrated the feasibility of the proposed method. Obviously, to meet various sorting accuracy requirements in an commercial application, the sorting threshold values would

Table 4
Performance of the algorithm of classifying stem-ends from normal and defective peels.

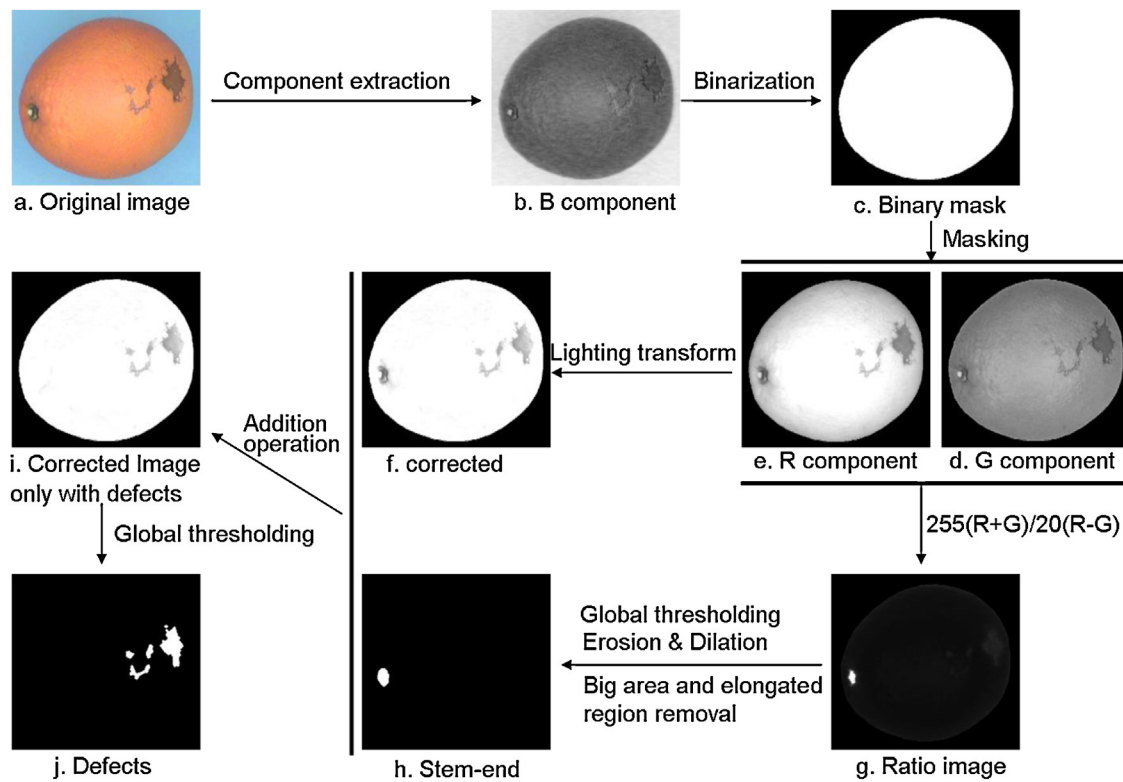| Actual group	Classified as			Correct classification (%)
	Normal and defective peel	Stem-end	Total	
Normal and defective peel	312	0	312	100%
Stem-end	0	168	168	100%
Total	312	168	480	100%

Fig. 11. Flow chart of the key steps involved in defects detection algorithm.

Table 5
Recognition rates for 720 independent test images including sound peels and defective skins under three representative thresholds.

Type of peel		Total images	Threshold $T_1 = 175$			Threshold $T_2 = 230$			Threshold $T_3 = 240$		
			Detection	Detection rate (%)		Detection	Detection rate (%)		Detection	Detection rate (%)	
Slight	Wind scarring	90	0	0	2.2	80	88.9	94.4	88	97.8	99.0
	Thrips scarring	90	2	2.2	(97.8)	84	93.3		86	95.6	
	Scale infestation	90	3	3.3		86	95.6		90	100.0	
	Copper burn	90	3	3.3		90	100.0		90	100.0	
Serious	Dehiscent fruit	90	90	100.0	97.0	90	100.0	100.0	90	100.0	
	Anthracnose	90	90	100.0		90	100.0		90	100.0	
	Canker spot	90	82	91.1		90	100.0		90	100.0	
Sound	Sound peel	90	90	100.0		90	100.0		88	97.8	
Total	8	720	360	50.0		700	97.2		712	98.9	

have to be carefully determined and adjusted. One drawback of the proposed algorithm is that it cannot sort oranges according to the type of defects. The methodology for identifying the type of each defect can be found in Blasco et al. (2007b).

Processing time of per Image 640×480 with a resolution of 0.28 mm per pixel is approximately 0.437 s (using a Pentium Dual CPU E2220 @ 2.40 GHz processor and 1024 Mb of RAM). Although this is still too much time to be implemented in a commercial system, which typically requires a processing time below 100 ms per image, optimization of this algorithm is currently being explored.

It should also be noted that the R component in this study on oranges was selected due to it having more distinct contrast between the defective regions and the sound skin compared to gray images. However, this conclusion does not mean that the R component image would be the best for all types of fruits. Therefore, the selection of the best RGB component is critical for effective implementation of the method. The selection of the best of the RGB components should be determined from original uncorrected images with the defective areas in the image being visually detected even with non-uniform lighting.

5. Conclusions

In this paper, a novel and practical lighting transform method was developed for correcting the adverse effects produced by the curvature of spherical fruit in acquiring images with a computer vision system. The algorithm was tested using the independent images of 4270 marked defects and 251 marked stem-ends and succeeded in segmenting 93.1% of defects and 100% of stem-ends. However, it was ineffective to discriminate stem-ends from true defects. To solve this problem, a stem-end identification algorithm was also introduced in this study. Finally, a combined algorithm was developed from the two methods. The combination algorithm could segment defects from normal fruit peels and it also could avoid the negative effects of stem-ends. Results with a 98.9% detection rate based on 720 independent sample images showed that the combination algorithm was effective in differentiating normal and defective oranges. Different sorting requirements could be met by properly selecting among the threshold values (T_1, T_2, and T_3). The technique generated from this research can be used in a commercial machine vision orange-defect-sorting system, but reducing the

processing time remains a challenge. Therefore, further optimization of the algorithm is necessary.

In addition, the basic assumption in this research for implementing the lighting transform method was that the acquired images can be decomposed into illumination and reflectance components. The lighting component represents low frequency, while the reflectance component represents higher frequency. So, the algorithm may work well for those fruits that have a relatively uniform color distribution on the surface, as orange samples used in this study. However, other types of fruits have varying surface colors and the effectiveness of the algorithm on them will require further research.

Acknowledgement

References

Aleixos, N., Blasco, J., Navarrón, F., Moltó, E., 2002. Multispectral inspection of citrus in real-time using machine vision and digital signal processors. Comput. Electron. Agric. 33, 121–137.

Balasundaram, D., Burks, T.F., Bulanon, D.M., Schubert, T., Lee, W.S., 2009. Spectral reflectance characteristics of citrus canker and other peel conditions of grapefruit. Postharvest Biol. Technol. 51, 220–226.

Bennedsen, B.S., Peterson, D.L., 2005. Performance of a System for Apple Surface Defect Identification in Near-infrared Images. Biosyst. Eng. 90, 419–431.

Blasco, J., Aleixos, N., Moltó, E., 2007a. Computer vision detection of peel defects in citrus by means of a region oriented segmentation algorithm. J. Food Eng. 81, 384–393.

Blasco, J., Aleixos, N., Gómez, J., Moltó, E., 2007b. Citrus sorting by identification of the most common defects using multispectral computer vision. J. Food Eng. 83, 384–393.

Blasco, J., Moltó, E., 2002. Identification of defects in citrus skin using multispectral imaging. In: International Conference on Agricultural Engineering, AgEng 02, Budapest, Hungary, EurAgEng Paper No. 02-AE-031.

Crowe, T.G., Delwiche, M.J., 1996a. Real-time defect detection in fruit: Part I. Design concepts and development of prototype hardware. Trans. ASAE 39, 2299–2308.

Crowe, T.G., Delwiche, M.J., 1996b. Real-time defect detection in fruit. Part II. An algorithm and performance of a prototype system. Trans. ASAE 39, 2309–2317.

Gonzalez, R.C., Woods, R.E., 2010. Digital Image Processing, 3rd ed. Publishing house of electronics industry, Beijing, China.

Gómez-Sanchis, J., Gómez-Chova, L., Aleixos, N., Camps-Valls, G., Montesinos-Herrero, C., Moltó, E., Blasco, J., 2008. Hyperspectral system for early detection of rottenness caused by Penicillium digitatum in mandarins. J. Food Eng. 89, 80–86.

Kim, D.G., Burks, T.F., Qin, J.W., Bulanonm, D.M., 2009. Classification of grapefruit peel diseases using colour texture feature analysis. Int. J. Agric. & Biol. Eng. 2, 41–50.

Kleynen, O., Leemans, V., Destain, M.F., 2005. Development of a multi-spectral vision system for the detection of defects on apples. J. Food Eng. 69, 41–49.

Leemans, V., Magein, H., Destain, M.F., 1998. Defects segmentation on 'Golden Delicious' apples by using colour machine vision. Comput. Electron. Agric. 20, 117–130.

Leemans, V., Destain, M.F., 2004. A real-time grading method of apples based on features extracted from defects. J. Food Eng. 61, 83–89.

Li, Q.Z., Wang, M.H., Gu, W.K., 2002. Computer vision based system for apple surface defect detection. Comput. Electron. Agric. 36, 215–223.

López-García, F., Andreu-García, G., Blasco, J., Aleixos, N., Valiente, J., 2010. Automatic detection of skin defects in citrus fruits using a multivariate image analysis approach. Comput. Electron. Agric. 71, 189–197.

Qin, J.W., Burks, T.F., Ritenour, M.A., Bonn, W.G., 2009. Detection of citrus canker using hyperspectral reflectance imaging with spectral information divergence. J. Food Eng. 93, 183–191.

Recce, M., Plebe, A., Taylor, J., Tropiano, G., 1998. Video grading of oranges in real time. Artif. Intell. Rev. 12, 117–136.

Sarker, N., Wolfe, R.R., 1985. Computer vision based system for quality separation of fresh market tomatoes. Trans. ASAE 28, 1714–1718.

Tao, Y., 1996. Spherical transform of fruit images for on-line defect extraction of mass objects. Opt. Eng. 35, 344–350.

Tao, Y., Wen, Z., 1999. An adaptive spherical image transform for high-speed fruit defect detection. Trans. ASAE 42, 241–246.

Throop, J.A., Aneshansley, D.J., Upchurch, B.L., Anger, B., 2001. Apple orientation on two conveyors: performance and predictability based on fruit shape characteristics. Trans. ASAE 44, 99–109.

Unay, D., Gosselin, B., 2007. Stem and calyx recognition on 'Jonagold' apples by pattern recognition. J. Food Eng. 78, 597–605.

Wen, Z., Tao, Y., 2000. Dual-camera NIR/MIR imaging for stem-end/calyx identification in apple defect sorting. Trans. ASAE 43, 449–452.

Xing, J., Bravo, C., Jancsok, P.T., Ramon, H., Baerdemaeker, J.D., 2005. Detecting bruises on 'Golden Delicious' apples using hyperspectral imaging with multiple wavebands. Biosyst. Eng. 90, 27–36.

Yang, Q., 1996. Apple stem and calyx identification with machine vision. J. Agric. Eng. Res. 63, 229–236.

Yang, Q., 1993. Finding stem and calyx of apples using structured lighting. Comput. Electron. Agric. 8, 31–42.

Ying, Y., Jing, H., Tao, Y., Zhang, N., 2003. Detection stem and shape of pears using Fourier transformation and an artificial neural network. Trans. ASAE 46, 157–162.

Zhu, B., Jiang, L., Tao, Y., 2007. Three-dimensional shape enhanced transform for automatic apple stem-end/calyx identification. Opt. Eng. 46, 1–9.